JOURNAL OF GEOPHYSICAL RESEARCH, VOL. 113, D11118, doi:10.1029/2007JD009041, 2008



# On the information content of the thermal infrared cooling rate profile from satellite instrument measurements

D. R. Feldman,[1] K. N. Liou,[2] R. L. Shia,[3] and Y. L. Yung[3]

Received 4 June 2007; revised 25 January 2008; accepted 25 February 2008; published 13 June 2008.

[1] This work investigates how remote sensing of the quantities required to calculate clear-sky cooling rate profiles propagates into cooling rate profile knowledge. The formulation of a cooling rate profile error budget is presented for clear-sky scenes given temperature, water vapor, and ozone profile uncertainty. Using linear propagation of error analysis, an expression for the cooling rate profile covariance matrix is given. Some of the features of the cooling rate covariance matrix are discussed, and it is found that nonzero error correlations in the temperature, water vapor, and ozone retrieval profiles must be considered to produce an unbiased estimate of cooling rate profile variance and the covariance structure. To that end, the exclusion of the details of this error correlation leads to an underestimation of the cooling rate profile uncertainty. This work then examines the assumptions made in the course of deriving the expression for the cooling rate covariance matrix by using ERA-40 Reanalysis data. It is established that the assumptions of linear error propagation and Gaussian statistics are generally tenable. Next, the information content of thermal infrared spectra with respect to clear-sky cooling rate profiles is investigated. Several formerly- and currently-operational spectrometers are compared with different spectral coverage, resolution, signal-to-noise ratio. Among these, IASI is found to have the ability to provide the greatest amount of information on the cooling rate profile. Also, it may be scientifically useful to develop far-infrared missions in terms of cooling rate profile analysis.

**Citation:** Feldman, D. R., K. N. Liou, R. L. Shia, and Y. L. Yung (2008), On the information content of the thermal infrared cooling rate profile from satellite instrument measurements, *J. Geophys. Res.*, *113*, D11118, doi:10.1029/2007JD009041.

## 1. Introduction

[2] Heating and cooling rate profiles are influenced by absorption, emission, and scattering by atmospheric state constituents such as water vapor ($H_2O$), carbon dioxide ($CO_2$), ozone ($O_3$), oxygen ($O_2$), methane ($CH_4$), nitrous oxide ($N_2O$), and liquid and ice clouds. Aerosols have a strong influence on radiative heating in the visible and near infrared portions of the spectrum and have a small impact on the infrared cooling rates where aerosol optical depth is high. Heating and cooling rate profile calculations are ubiquitous in the course of general circulation model (GCM) runs which utilize correlated-*k* (or other band-model) methods because these algorithms provide computational efficiency and achieve reasonable accuracy with respect to line-by-line calculations for the same inputs of temperature, water vapor, ozone, and cloud optical depth profiles. An in-depth discussion of heating rate profile calculation both from a theoretical and practical standpoint can be found in texts such *Goody and Yung* [1989] and *Liou* [2002].

[3] Radiometric accuracy with respect to line-by-line models is crucial to many aspects of model performance because diabatic heating affects circulation. *Morcrette* [1990] found that an improved radiative transfer algorithm resulted in substantial changes to the distribution of radiative energy in the ECMWF forecast model while *Iacono et al.* [2000] explored how the introduction of an improved correlated-*k* algorithm to the CCM3 model changed resulting cooling rates and fluxes which partially ameliorated the model's cold bias at high latitudes. In general, line-by-line codes are in good agreement with each other [*Kratz et al.*, 2005] though comparisons of GCM heating rate calculations still exhibit discrepancies related to band-model parameterizations [*Ellingson and Fouquart*, 1991; *Baer et al.*, 1996; *Collins et al.*, 2006].

[4] Meanwhile, large-scale retrieval efforts from satellite-borne instruments produce the inputs necessary to calculate fluxes and heating rate profiles: these products include temperature, water vapor, and ozone profiles and other trace gas descriptions along with some description of cloud cover [e.g., *Qu et al.*, 2001; *Susskind et al.*, 2006; *Barnet et al.*, 2003; *Li et al.*, 2005]. Several authors have explored the determination of fluxes such as OLR and total surface

[1]Department of Environmental Science and Engineering, California Institute of Technology, Pasadena, California, USA.
[2]Department of Atmospheric and Oceanic Sciences, University of California-Los Angeles, Los Angeles, California, USA.
[3]Division of Geological and Planetary Sciences, California Institute of Technology, Pasadena, California, USA.


0148-0227/08/2007JD009041$09.00

downwelling flux (more easily measurable quantities) from remote sensing products [e.g., *Zhang et al.*, 1995, 2004]. Nevertheless, there have been only a few papers focused on how well-suited these products are for determining heating and cooling rates. *Mlynczak et al.* [1999] provided a comprehensive assessment of stratospheric radiative balance by using remote sensing data. Efforts to utilize International Satellite Cloud Climatology Program data to calculate monthly radiative fluxes and heating rates and the associated sensitivity of such calculations were explored by *Bergman and Hendon* [1998]. More recently, there has been renewed focus on assessing heating rates using data from ground validation sites [*Fueglistaler and Fu*, 2006; *McFarlane et al.*, 2007]. Also, heating rates derived from operational analysis temperature, water vapor, and ozone data, in combination with cloud profiling radar data, are currently being released as a standard product associated with the CloudSat mission [*L'Ecuyer*, 2007]. If properly implemented, the patterns of heating rates derived from remote sensing data can be compared with those calculated by models in a state-space that summarizes the interlayer radiative energy exchange as it pertains to the primitive equations. In principle, if all of the inputs to the heating rate calculation are known with certainty, the radiometric accuracy of the band-model with respect to line-by-line calculations and spectroscopic misrepresentation are the only appreciable sources of error. However, remote sensing retrievals produce an imperfect estimation of the true quantity being retrieved, and it is important to assess how these imperfections relate to heating and cooling rate knowledge.

[5] In order to bridge the gap between satellite-based remote-sensing measurements and the heating and cooling rates on which circulations models rely, preliminary efforts to address the correspondence between radiances and cooling rates have been made [*Liou and Xue*, 1988; *Feldman et al.*, 2006], though formal error analyses have been undertaken sparingly. Those papers discuss methods for retrieving cooling rates from radiance data, and the latter paper utilizes several AIRS spectra [*Aumann et al.*, 2003] to demonstrate feasibility. Given the existence of several different instruments for atmospheric sounding, it is reasonable to explore metrics for understanding which instruments best constrain heating/cooling rates. To this end, it is necessary to produce a formal error budget and discuss the hyperspectral instrument specifications that most effectively reduce uncertainty in heating/cooling rate knowledge. Therefore, this paper focuses on establishing straightforward, computationally-efficient methods for making appropriate estimation of the cooling rate covariance matrix so that the skill of standard retrieval products and methods can be evaluated in the context of cooling rates. While shortwave heating rates are also important to circulation models, this paper will generally focus on tropical longwave cooling rates associated with different temperature, water vapor, and ozone profiles due to timely scientific interest [i.e., *Hartmann et al.*, 2001; *Sherwood and Dessler*, 2001; *Gettelman et al.*, 2004].

[6] The concept of information content is broadly applied throughout this paper. Formally originating with *Fisher* [1925] and elaborated substantially by *Shannon* [1948], this is a useful concept for describing the change in knowledge as the result of a measurement of a set of quantities that may or may not be independent. The information content of a set of measurements is equivalent to the same number of measurements of independent equal probability binary events. Another interpretation of information content is that it describes the number of different states that can be distinguished by a measurement. When used properly, information content is an absolute currency for the evaluation of retrieval system design that produces a reliable metric with which optimization can occur on many fronts simultaneously.

[7] This paper is organized as follows. In section 2, we discuss the basic molecular bands and their cooling rates using the template of the Tropical Model Atmosphere [*Anderson et al.*, 1986]. Then, we move on to describe sources of uncertainty in determining cooling rate profiles and cooling rate variability in the tropics. In section 3, formal error propagation analysis is applied to the study of cooling rates given expected a priori and aposteriori uncertainties in the clear-sky inputs. This propagation of error analysis is then applied to reanalysis data to demonstrate the efficacy of this approach in determining cooling rate covariance matrices. Finally, section 4 provides context for the treatment of the intersection between cooling rate profiles and remote sensing measurements with the comparison of the cooling rate information content associated with several past and current spectrometers.

## 2. Sample Case and Sources of Uncertainty

[8] This paper utilizes radiative transfer codes from the AER suite (http://rtweb.aer.com): for line-by-line radiative transfer calculations to produce radiance, the Line-by-Line Radiative Transfer Model, LBLRTM, [*Clough et al.*, 1992, 2005; *Clough and Iacono*, 1995] version 9.3 is used, for line-by-line flux and heating-rate calculations, RADSUM version 2.4 is used, and for correlated-$k$ calculations, the Rapid Radiative Transfer Model (RRTM) including longwave (version 3.01) and shortwave (version 2.5) modules are used [*Iacono et al.*, 2000; *Mlawer et al.*, 1997]. For heating rate profile calculations, RRTM is accurate to within 0.1 K/d in the troposphere and 0.3 K/d in the stratosphere relative to line-by-line calculations (see *Mlawer et al.* [1997] for details).

[9] A sample cooling rate profile calculated with RRTM is shown in Figure 1. Here, nine spectral bands are presented along with the total IR cooling rate profile given the Tropical Model Atmosphere. The three far-infrared bands covering 10–630 $cm^{-1}$ show significant upper tropospheric cooling which arises from the rotational band of water vapor. In fact, these far-infrared bands, for which no global satellite-based direct measurements currently exist, account for upwards of 90% of cooling in the upper troposphere in the tropics. The two bands from 630–820 $cm^{-1}$ are dominated by the $\nu_2$ band of $CO_2$ which contributes significantly to stratospheric cooling rates. The two spectral bands from 820–980 $cm^{-1}$ and 1080–1180 $cm^{-1}$ show the cooling in the window bands which is strongly influenced by water vapor continuum absorption. The 985–1085 $cm^{-1}$ spectral region is affected by the $\nu_3$ band of $O_3$ and the 1070–1180 $cm^{-1}$ region is influenced by the $\nu_1$ band of $O_3$ [*Clough and Kneizys*, 1966]. Both of these bands produce

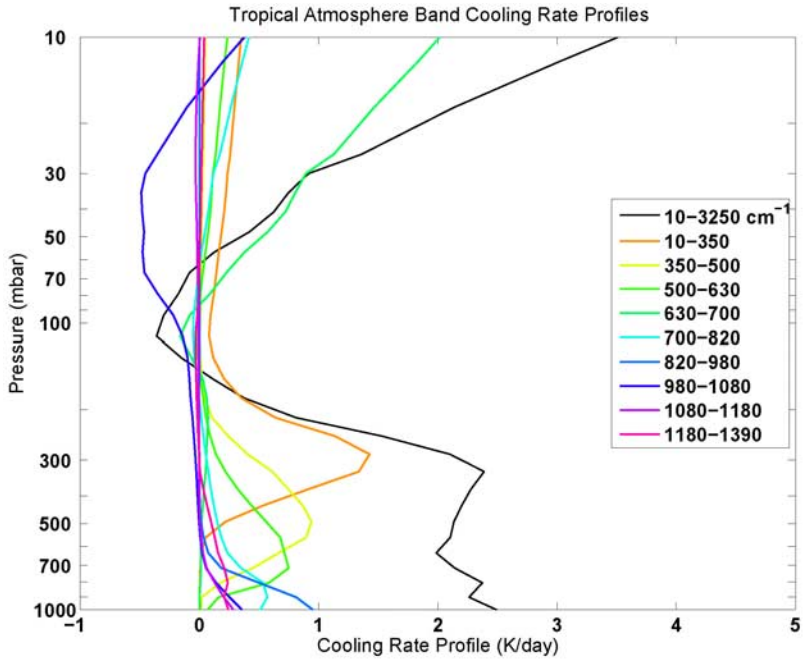


**Figure 1.** Total and band-averaged IR cooling rate profiles for the Tropical Model Atmosphere on a log-pressure scale.

IR heating in the lower stratosphere which arises from the rapid vertical change in $O_3$ concentration and the corresponding drop in interlayer transmittance. These bands also lead to IR cooling in the midddle and upper-stratosphere with radiation to space.

[10] A demonstration of the zonal, meridional, and temporal variability in total IR cooling rate profiles due to the corresponding variability in the temperature, water vapor, and ozone fields gives an indication of the appropriate scale for a priori values and constraints for cooling rate profile analysis. Data from year 2000 of the European Centre for Medium Range Weather Forecasts (ECMWF) 40-year reanalysis (ERA-40) [*Uppala et al.*, 2005] have been utilized for this purpose as inputs to RRTM, which happens to be essentially the same radiative transfer code that the ERA-40 program utilizes internally. The reanalysis reports temperature, water vapor, and ozone at 23 sigma levels ranging from the surface to around 1 mbar at 6-h intervals. As seen in Figure 2a, the total IR cooling rate profile at low latitudes is several K/d in the troposphere, decreases to much less than 1 K/d in the tropopause region, and rises rapidly in the stratosphere to around 10 K/d near the stratopause. For higher latitudes, cooling rates are more uniform from the free troposphere to the lower stratosphere and rise rapidly in the middle and upper-stratosphere. Figure 2b shows the temporal standard deviation of the cooling rate profile across a zonal band located at the equator over using reanalysis data from January 2000 with tropospheric variability ranging from several tenths of a K/d in the troposphere to around 0.1 K/d at the tropopause and around 0.5 K/d in the middle stratosphere. Figure 2c displays a meridional cross-section of the temporal variability in the cooling rate profile and shows comparable magnitude to Figure 2b.

[11] A cooling rate profile calculation requires knowledge of the interlayer transmission profile in the band of interest along with the temperature profile. For clear-sky calculations, uncertainty arises from the lack of knowledge of the temperature profile, the vertical distribution of absorbing/emitting species, and also from spectroscopic uncertainty largely limited to continua models. The water vapor continuum has been shown to be very significant for the determination of cooling rate profiles at many different altitudes [*Iacono et al.*, 2000]. However, the incorporation of a state-of-the-art, semi-empirical model [*Clough et al.*, 2005] into many modern cooling rate calculations largely removes this as a source of systematic error.

## 3. Error Propagation and Covariance Matrices

[12] Operational heating and cooling rate calculation algorithms generally do not include formal error estimates as a result of the uncertainty in input parameters such as the temperature, water vapor, ozone, and cloud profiles. Finite difference uncertainty estimation is sometimes employed for gross error statistics [*Mlynczak et al.*, 1999]. However, formal error estimates can establish how uncertainties in atmospheric state descriptors such as the temperature, water vapor, and ozone profiles and cloud layering propagate into uncertainties both in spectral and broadband cooling rate profiles. This calculation will involve the mapping of the atmospheric state covariance matrix onto the cooling rate covariance matrix. For this mapping, we recognize that a deviation in an atmospheric state value in one layer will tend to impact the cooling rate profile at that layer *and* at neighboring layers also. Figure 3 shows the result of a perturbation in a single atmospheric layer of the temperature value or the water vapor or ozone concentration. Here, the results of three separate perturbations to the atmospheric state for the layer from 14 to 16 km (182–132 mbar) are shown: the temperature is increased by 1 K, the water vapor

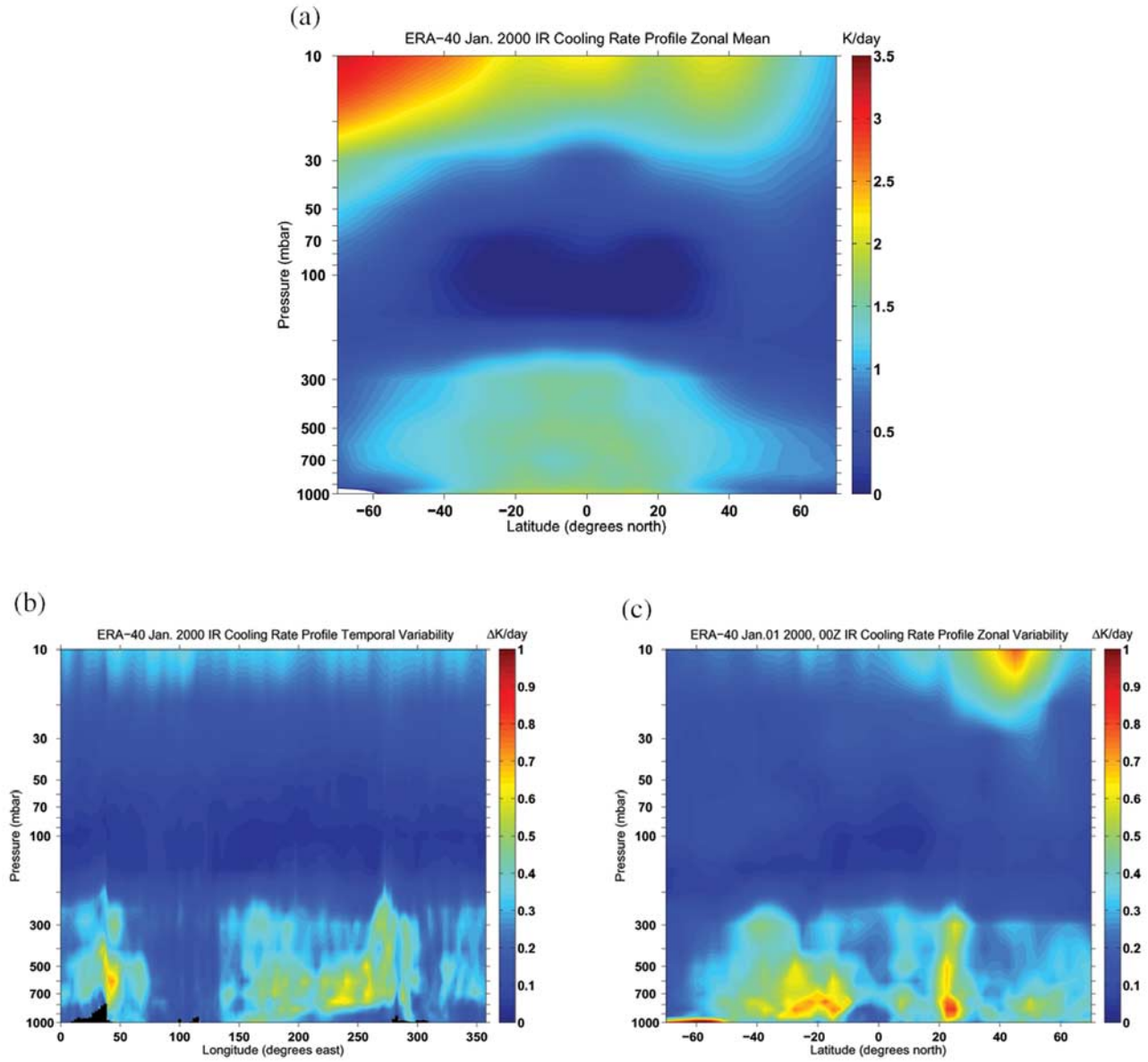


**Figure 2.** (a) Contours of clear-sky total IR cooling rate profile values from monthly averaged ERA-40 reanalysis data for January 2000. (b) Meridional cross-section of temporal variability in clear-sky total IR cooling rate at the equator using 6-h ERA-40 reanalysis data for January 2000. (c) Same as Figure 2b but displaying a zonal cross-section of temporal variability.

value is increased by 5%, and the ozone value is increased by 5%. Note that as a result of a positive perturbation in the temperature and water vapor in a certain layer, the cooling rate in that layer increases and the cooling rate in adjacent layers generally decreases as a result of increased emission from the perturbation layer. Also, for increases in water vapor, the optical path of the perturbed layer increases, thereby decreasing the cooling to space of the layers below perturbed layer. A positive perturbation in ozone in the troposphere leads to different results: this perturbation causes increased IR *heating* in that layer and it decreases IR heating in the upper troposphere/lower stratosphere (UTLS), even if the perturbation layer is not-necessarily near the UTLS. This behavior arises because ozone IR heating in the UTLS results from the rapid increase of $O_3$ with height. In a spectral region that is otherwise free of significant absorptions between the surface and the UTLS, a typical $O_3$ profile leads to a change of interlayer transmittance from the $O_3$ $\nu_3$ and $\nu_1$ bands. Any positive increase in the $O_3$ concentration leads to increased IR heating in the perturbation layer. However, the response of the total IR cooling rate profile to similar perturbations at other layers leads to qualitatively and quantitatively different results depending on which bands contribute to the cooling and whether cooling-to-space dominates.

[13] Clearly, the propagation of uncertainties in conventional atmospheric state parameters such as the T, $H_2O$, and $O_3$ profiles as they pertain to the cooling rate covariance structure is nontrivial. We seek to characterize the cooling rate covariance matrix because it is a useful concept as

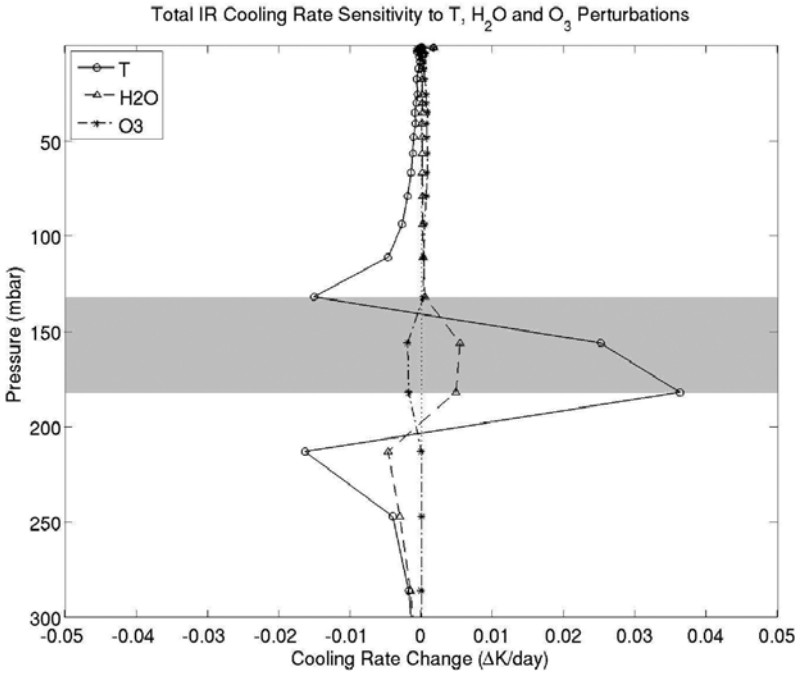


**Figure 3.** Change in Tropical Model Atmosphere total IR cooling rate profile arising from separate perturbations in the layer from 132 to 182 mbar of +1 K in temperature and +5% in $H_2O$ and $O_3$ volume mixing ratio. Gray shading indicates the perturbation layer.

applied to the retrieval of profile quantities from remote sensing data: it describes how errors are correlated between different entries of the profile. In order to account for the extent to which uncertainties in atmospheric state parameters at all layers impact knowledge of the cooling rate at the layer of interest, we start with linear error propagation for a function of several normally-distributed random variables:

$$[\Delta f]^2 = \sum_{i=1}^{n}\sum_{j=1}^{n}\frac{\partial f}{\partial x_i}\frac{\partial f}{\partial x_j}\mathrm{cov}(x_i, x_j) \tag{1}$$

where *cov* refers to the covariance function to describe the error correlations in a quantity $f$ that is a function of several variables for which there is nonzero covariance among input variables ($x_1, \ldots x_n$) [*Taylor and Kuyatt*, 1994].

[14] To calculate the diagonal of the cooling rate profile covariance matrix, we apply equation (1) to the cooling rate value in each layer:

$$\left[\Delta\dot{\theta}(z)\right]^2 = \sum_{i=1}^{n}\sum_{j=1}^{n}\frac{\partial\dot{\theta}(z)}{\partial x_i}\frac{\partial\dot{\theta}(z)}{\partial x_j}\mathrm{cov}(x_i, x_j) \tag{2}$$

where ($x_1, \ldots x_n$) represent all of the atmospheric state inputs that are relevant to cooling rate profile calculations at each layer and $\dot{\theta}$ refers to either the spectral or broadband cooling rate at height $z$. In order to calculate the off-diagonal elements of the cooling rate profile covariance matrix, we note the following relationship between the variance of a sum of two quantities:

$$\mathrm{var}(x+y) = \mathrm{var}(x) + \mathrm{var}(y) + 2\mathrm{cov}(x, y) \tag{3}$$

from which we find:

$$\mathrm{cov}\left[\dot{\theta}(z_i), \dot{\theta}(z_j)\right] = \frac{1}{2}\{\mathrm{var}\left[\dot{\theta}(z_i) + \dot{\theta}(z_j)\right] - \mathrm{var}\left[\dot{\theta}(z_i)\right] - \mathrm{var}\left[\dot{\theta}(z_j)\right]\} \tag{4}$$

where the first term on the RHS of the above equation is given by:

$$\mathrm{var}\left[\dot{\theta}(z_i) + \dot{\theta}(z_j)\right] = \sum_{k=1}^{n}\sum_{m=1}^{n}\frac{\partial\left[\dot{\theta}(z_i) + \dot{\theta}(z_j)\right]}{\partial x_k}\frac{\partial\left[\dot{\theta}(z_i) + \dot{\theta}(z_j)\right]}{\partial x_m} \cdot \mathrm{cov}(x_k, x_m) \tag{5}$$

and the other terms on the RHS of equation (4) were derived from equation (2). In this formulation, it should be noted that $\dot{\theta}(z_i)$ and $\dot{\theta}(z_j)$ can refer to cooling rates associated with different layers and different spectral regions. With equations (2) and (4), we can populate a covariance matrix with respect to the cooling rate profile given the covariance matrix of the atmospheric state parameters. In order to implement equation (2) numerically, finite difference perturbations are applied to the T, $H_2O$, and $O_3$ profiles separately to produce cooling rate profile difference values (Jacobians). The implementation of the derivative terms in equation (5) simply requires summing the finite difference values calculated for equation (2).

[15] An application of this formal error budget analysis to cooling rate profile calculations is demonstrated with the RRTM calculation of band cooling rate profile errors for the Tropical Model Atmosphere [*Anderson et al.*, 1986]; here, the standard deviation in the temperature profile is 3 K in each layer (spaced approximately 1 km apart) and that of the

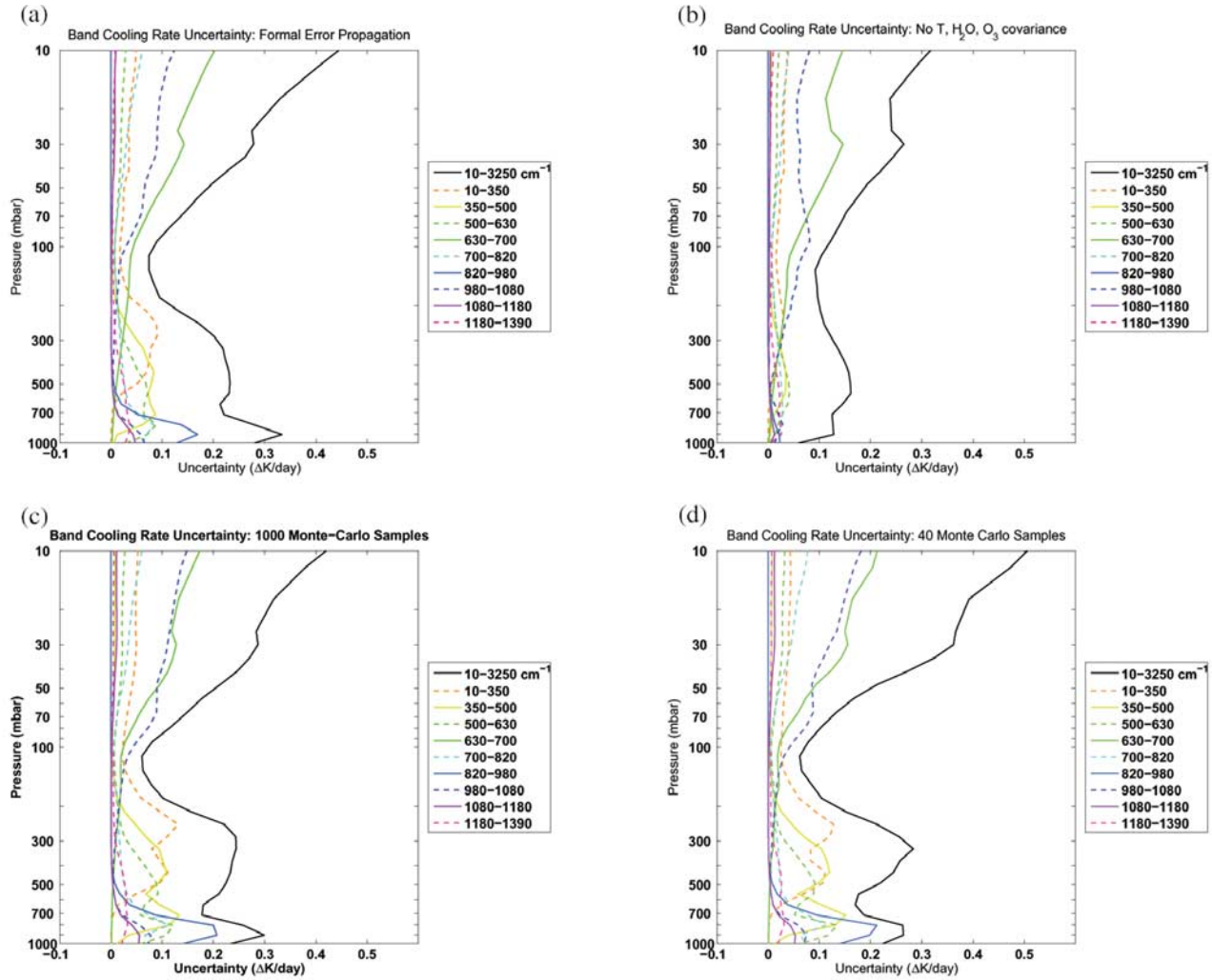


**Figure 4.** (a) Error estimation for the total and band-averaged IR cooling rate profile using formal error propagation as described in equations (2) and (4) with T uncertainty at 3 K/km and $H_2O$ and $O_3$ uncertainty at 20% vmr/km where T, $H_2O$, and $O_3$ errors covary according to equation (6). (b) Same as Figure 4a but T, $H_2O$, and $O_3$ errors are uncorrelated. (c) Error bars estimated from 1000 Monte Carlo perturbations to the T, $H_2O$, and $O_3$ profiles. (d) Same as Figure 4c but using 40 Monte Carlo perturbations.

water vapor and ozone profiles is 20% of their respective values in each layer. The purpose of this exercise is to characterize cooling rate variability from T, $H_2O$, and $O_3$ variability and set reasonable a priori constraints on the cooling rate from an assumed climatology for subsequent analysis. The a priori covariance of the temperature, water vapor, and ozone profiles is assumed to be based on a first-order autoregressive process such that adjacent layer errors are correlated [*Rodgers*, 2000]. Consequently, each element of this covariance matrix is given by:

$$\mathrm{cov}(x_i, x_j) = \sigma(x_i)\sigma(x_j)\exp\left(-\frac{|z_i - z_j|}{H}\right) \qquad (6)$$

where $x_i$ and $x_j$ refer to different layer quantities, $\sigma(x_i)$ refers to the standard deviation in $x_i$, $z_i$ and $z_j$ refer to the altitude of each layer, and $H$ is the atmospheric pressure scale height. The true covariance matrix of $H_2O$ and $O_3$ will be undoubtedly of a quantitatively different nature and such profile quantities as T and $H_2O$ are undoubtedly correlated to some extent. For the purposes of illustrating the mapping of T, $H_2O$, and $O_3$ covariance matrices to the cooling rate covariance matrix, however, we assume in the *a priori* sense that the T-$H_2O$, T-$O_3$, and $H_2O$-$O_3$ covariances are exactly zero. From Figure 4a, it can be seen that this propagation of uncertainty analysis leads to some predictable and some surprising results.

[16] From a qualitative point of view, we find that uncertainty in the distribution of water vapor contributes most substantially to the total cooling rate profile uncertainty in the troposphere as shown with the contributions from the far-infrared. In the stratosphere, uncertainty in the total IR cooling rate profile arises from uncertainty in the $O_3$ $\nu_3$ and $\nu_1$ bands and the $CO_2$ $\nu_2$ band cooling; the former term is determined by $O_3$ and T profile uncertainty while the latter term is determined only by T profile uncertainty. In

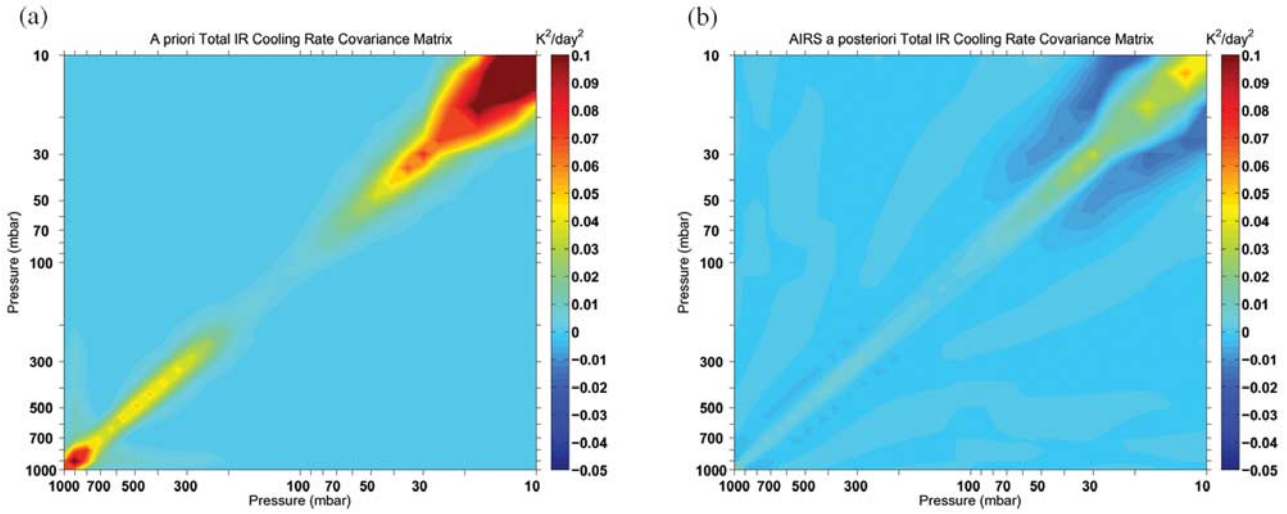


**Figure 5.** Total IR cooling rate covariance matrices with the Tropical Model Atmosphere for (a) a priori uncertainty of T at 3 K/km and $H_2O$ and $O_3$ uncertainty at 20% vmr/km where T, $H_2O$, and $O_3$ errors covary according to equation (6). (b) a posteriori uncertainty with a standard retrieval of T, $H_2O$, and $O_3$ profiles using the AIRS instrument model.

the tropopause region, the total IR cooling rate uncertainty is largely composed of the $O_3$ $\nu_3$ and $\nu_1$ bands and the $CO_2$ $\nu_2$ band cooling uncertainty, and water vapor (from the rotational band and the $v_3$ band) uncertainty is not the dominant contributor.

[17] Another very important consideration from this analysis is to note the results shown in Figures 4a–4d with respect to uncertainty estimation. All figures show the estimation of total IR and also band-averaged cooling rate profile uncertainty. First, Figure 4a shows error estimation derived from equations (2) and (4) with off-diagonal covariance matrix components determined from equation (6). Figure 4b shows this estimation derived from formal uncertainty propagation as described above with no off-diagonal covariance matrix components (zero covariance between layers for T, $H_2O$, and $O_3$). Figure 4c shows the estimation of variability using 1000 Monte Carlo perturbations of the T, $H_2O$, and $O_3$ profiles assuming that the probability distribution functions (pdfs) of all variables are Gaussian. In these Monte Carlo simulations, the layer of the perturbation of the T, $H_2O$, and $O_3$ values is chosen from a uniformly-distributed random number and the magnitude and sign of the perturbation are determined by a normally-distributed random variable scaled by the estimated error in the perturbation layer. The correlation matrix derived from the covariance matrix is used to scale a profile of nonzero perturbations of the T, $H_2O$, and $O_3$ profiles so the simulation is authentic to the assumed covariance structure.

[18] From Figures 4a and 4b, it can be seen that the off-diagonal components of the T, $H_2O$, and $O_3$ covariance matrices tend to increase the derived variability in the cooling rate profile which implies that for remote sensing to be useful for cooling rate constraint, it is important to retain the details of the retrieval product error correlation structure. Also, the latter two panels show that the cooling rate error budget can be estimated through Monte Carlo simulations, though in practice, fewer than 1000 simulations are required to describe the cooling rate profile uncertainties. That is, Figure 4d shows the variability estimation using 40 Monte Carlo simulations which is qualitatively similar to the estimation shown in Figure 4c. It should be noted that the uncertainty shown in these four panels is much greater than the typical error that would be expected in the reanalysis results. Nevertheless, the purpose of these figures is to demonstrate different methods for estimating cooling rate uncertainty *given* T, $H_2O$, and $O_3$ uncertainty and the associated covariance matrix. Also relevant to this discussion is the sensitivity of the derived cooling uncertainty to the covariance terms of the T, $H_2O$, and $O_3$ covariance matrices. Particularly, we examined the sensitivity of the results shown in Figure 4a to the parameter $H$ in equation (6). We found that a decrease in $H$ by, for example, a factor of two, leads to an increase in the resulting cooling rate uncertainty at all levels approximately 10 percent.

[19] It should also be noted that this formal error propagation analysis for quantities that are derived directly from retrieval results can be applied to many other aspects of satellite instrument data analysis, especially with respect to higher-level retrievals using Bayesian geophysical inversions that directly apply to circulation models. Specifically, this analysis is also applicable to the understanding of cooling rate profiles under cloudy conditions with respect to the knowledge of cloud optical depth profiles.

[20] Whereas Figures 4a–4d show cooling rate profile standard deviations, the cooling rate covariance matrix in Figure 5a illustrates the propagation of temperature, water vapor, and ozone profile covariance into the covariance for the total IR cooling rate profile. The figure shows that the off-diagonal covariance matrix components generally decrease exponentially with vertical separation, and the long-range, weak covariance between cooling rates at different layers in the troposphere arises from the assumed long-range, weak covariance in the water vapor profile. Cooling rate profile variance in the stratosphere is much greater than in the troposphere due to stratospheric temperature and ozone uncertainty. The small off-diagonal covariance matrix

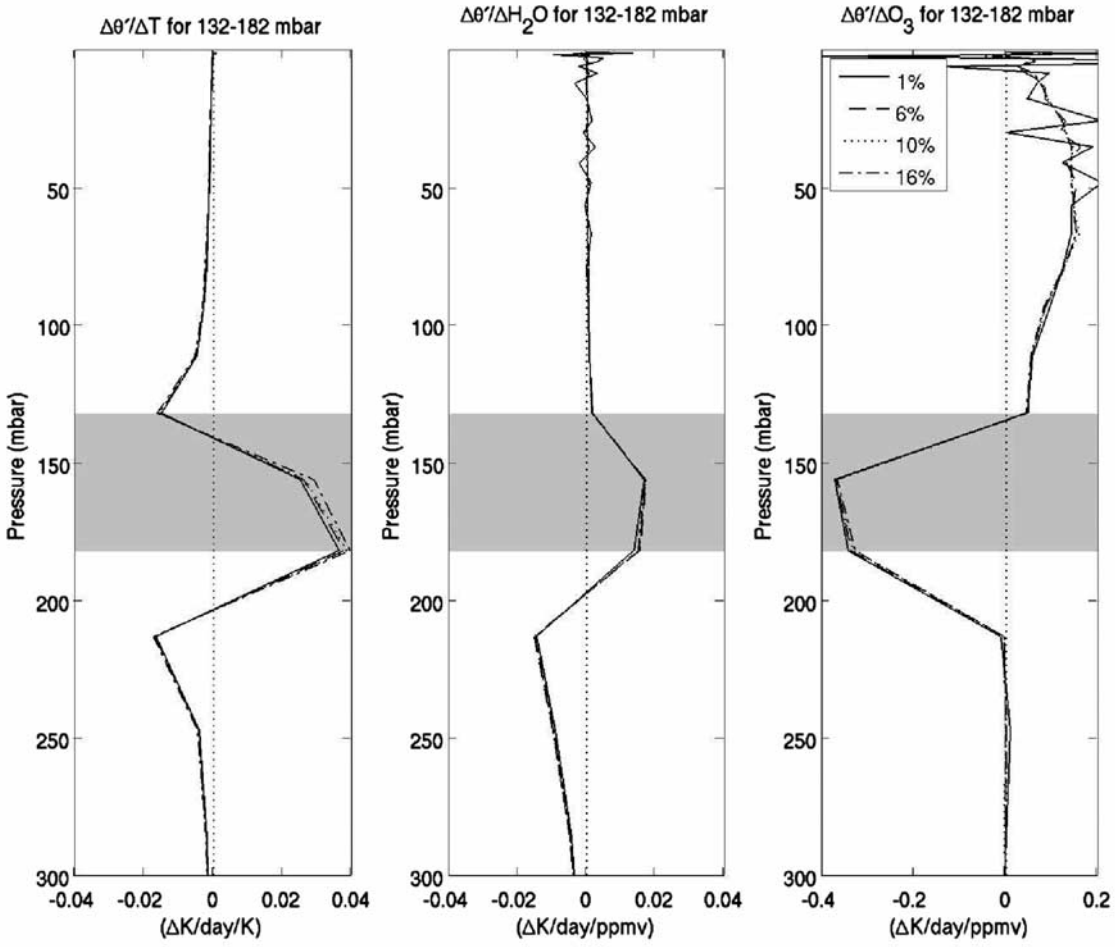


**Figure 6.** Finite difference Jacobian of cooling rate profile change with respect to changes in T (left), $H_2O$ (center), and $O_3$ (right) over the layer from 132–182 mbar. The linearity of the Jacobian is tested through different percentage change step sizes and these different step sizes are distinguished through the linestyles indicated by the legend in the right.

elements of the cooling rate profile in the stratosphere are caused by the larger altitude spacing between layers in the stratosphere which also leads to small off-diagonal covariance matrix components for stratospheric T and $O_3$ profiles.

[21] Figure 5b shows that the introduction of thermal sounder retrieval information produces an aposteriori covariance matrix that is qualitatively and quantitatively different from the a priori covariance matrix because the sounder measurement significantly improves understanding of those quantities required for the cooling rate profile calculation. First, the variance at all layers is significantly reduced after the measurement. This is to be expected since the T, $H_2O$, and $O_3$ profiles are better constrained after the measurement. Second, the limited number of degrees of freedom of the signal with respect to the temperature, water vapor, and ozone profiles is also evidenced in the aposteriori cooling rate covariance. That is, the retrieval has limited vertical resolution and thus imparts a set of independent pieces of information this is generally smaller than the number of retrieval quantities. The result is that the retrieved profile quantities tend to oscillate about the true profile quantities, and the cooling rate covariance matrix associated with such T, $H_2O$, and $O_3$ profile retrievals has negative covariance values in the near-range off-diagonal components. This negative covariance tends to reduce the effective vertical resolution of cooling rates that are derived from the spectrometer retrievals. If, for example, one is interested in the vertical structure of the cooling rate in the boundary layer, the vertical width of the T, $H_2O$, and $O_3$ retrieval averaging kernels will frustrate efforts for meaningful cooling rate analysis. Depending on the way in which cooling rates are utilized, vertical resolution may or may not be necessary. For example, the comparison of vertically-integrated tropospheric cooling resulting from different water vapor distributions may allow for degraded vertical resolution which can be accomplished by passing the high-resolution covariance matrix through a vertically-averaging operator. On the other hand, circulation models generally require high vertical resolution for heating/cooling rates, so analysis of cooling rates from sounder retrievals as compared to circulation model cooling rates should be undertaken at high resolution.

[22] The formulation of the cooling rate covariance matrix herein rests on several assumptions which need to be addressed. First, because significant cooling arises from the layer at which the atmosphere transitions between optical

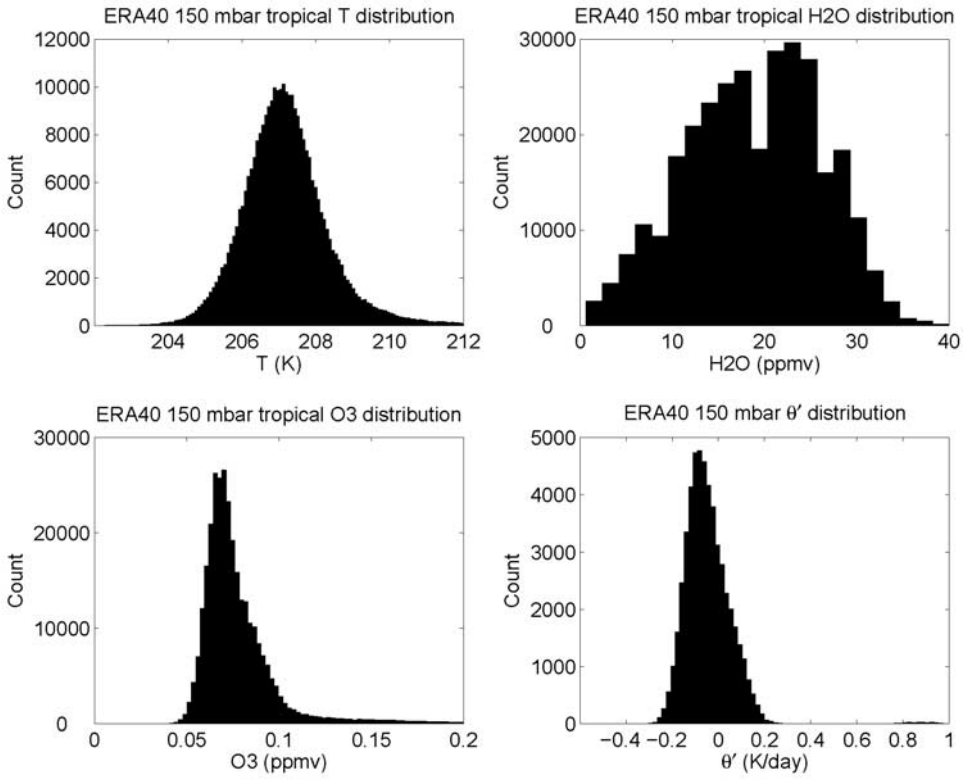


**Figure 7.** Sample probability distribution functions of the temperature (upper left), water vapor (upper right), ozone (lower left) and cooling rate (lower right) at 150 mbar from the ERA-40 data set for January 2000 for the region bounded by (20°S, 20°N) and (150°E, 210°E).

thickness and transparency in a certain band, the nonlinear nature of the radiative transfer equation may render the linear error analysis less meaningful. The issue here is whether this error propagation is valid for small changes in the clear-sky cooling rate inputs and what magnitude of T, $H_2O$, and $O_3$ profile uncertainty invalidates this linearity assumption. To estimate this, we investigate the behavior of the derivative terms in equation (2) by examining the change in a finite difference derivative approximation with increasing differential step size. The three panels of Figure 6 show the change in cooling rate for different perturbations in the temperature, water vapor, and ozone at 150 mbar normalized by the perturbation step size. It can be seen from this figure that even for fairly large perturbations, the normalized response of the clear-sky cooling rate profile does not change significantly (though RRTM has difficulty resolving the effects of small perturbations on stratospheric cooling rates). Even the nonlinearity shown in the T perturbation panel only becomes evident for changes on the order of 10% which represents a perturbation of over 20 K. Perturbations in other layers in the atmosphere are similar to the results in Figure 6 in that the finite difference Jacobians are nearly independent of step-size.

[23] The other important assumption in the derivation of a cooling rate covariance matrix is whether Gaussian statistics can be utilized. Since many of the physical quantities relevant to cooling rate profiles can be reasonably represented with Gaussian statistics and because error propagation in these instances can be described analytically, it is convenient to make an assumption that the probability distribution functions (pdfs) of all variables associated with the calculation of the cooling rate profile are normal. This may be reasonable given the low number of parameters required to constrain a Gaussian pdf, but this assumption can be tested. If the pdfs of the input variables are non-Gaussian, covariance matrix estimation from the approach described above may be difficult. The lack of an analytic expression (e.g., equation (1)) for meaningful error bars of functions with non-Gaussian inputs has led to diverse approaches some of which focus on Monte Carlo distribution sampling [e.g., *Palacios and Steel*, 2006; *Posselt et al.*, 2006]. Indeed, the error estimation in Figure 4a was qualitatively accomplished with a limited number of Monte Carlo samples as shown in Figure 4d.

[24] Testing the assumptions made in the course of the cooling rate covariance matrix formulation using real data or a realistic data set is important to establishing the utility of error propagation as it applies to cooling rate profiles. The ERA-40 reanalysis data fields provide a convenient, straightforward, and realistic set to calculate sample covariance matrices of T, $H_2O$, and $O_3$ profiles and also sample cooling rate covariance matrices. The pdfs of temperature for the region bounded by 20°S, 20°N and 150°E, and 210°E at most levels exhibit qualitatively Gaussian behavior though water vapor and ozone exhibit a much different distribution that can be better characterized as lognormal. The resulting pdfs of cooling rates at various layers are also qualitatively Gaussian with some positive skewness. An example of the pdfs of temperature, water vapor, ozone, and cooling rate at 150 mbar is shown in Figure 7. In order to

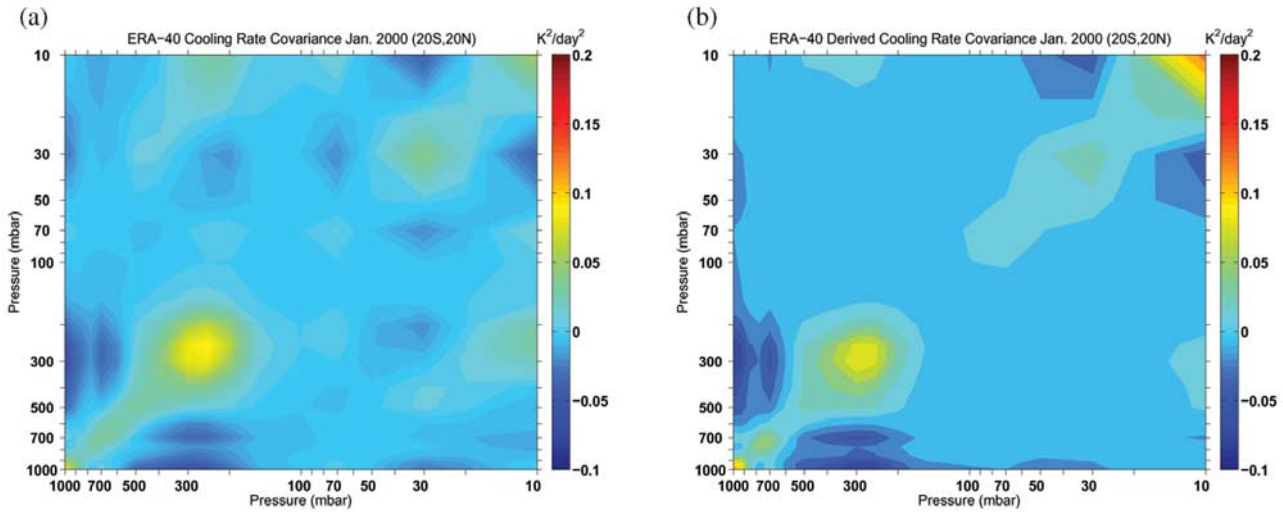


**Figure 8.** Clear-sky total IR cooling rate covariance matrix from ERA-40 reanalysis for the region bounded by (20°S, 20°N) and (150°E, 210°E) for January 2000 calculated from (a) ensemble cooling rate calculations and (b) error propagation analysis using calculated variability in T, $H_2O$, and $O_3$ fields.

estimate the cooling rate covariance matrix, it is more appropriate to utilize the covariance of the logarithm of $H_2O$ and $O_3$ and also the change in cooling rate profile with respect to changes in the logarithm of $H_2O$ and $O_3$.

[25] In Figure 8a, a cooling rate profile covariance matrix is calculated from an ensemble of clear-sky cooling rate profiles from all time steps of the ERA-40 in January 2000 from 20°S to 20°N and 150°E to 210°E. Figure 8b shows the cooling rate covariance matrix derived with equations (2–5) using calculated T, log($H_2O$), and log($O_3$) covariance matrices. That is, we are calculating the covariance matrix of T, log($H_2O$), and log($O_3$) from a large set of reanalysis profiles using error propagation as discussed above to produce a cooling rate covariance matrix. The results are compared to the covariance matrix derived empirically from the cooling rate profile calculations performed with the same set of T, $H_2O$, and $O_3$ profiles. The two covariance matrices describe variability and are qualitatively similar, though the latter (empirically-derived) has substantially more structure. The discrepancy arises primarily due to the non-Gaussian pdfs of the input quantities. Clearly, the series of assumptions necessary to create the cooling rate covariance matrix from equation (2) and equation (4), including Gaussian statistics and the validity of the linear error estimation for slightly or moderately nonlinear regimes, must be utilized with some caution.

## 4. Spectrometer Information Content Comparison

[26] Given a proper formulation for the cooling rate profile covariance matrix as a function of the atmospheric state covariance matrix, an information content analysis can be performed to assess the relative merits of traditional retrieval techniques using data from past, current, and future observing systems. Also, information content analysis facilitates discussion of the value of the traditional treatment of cooling rates and other approaches to the analysis of spectra. In the previous section, we developed methods for calculating the error budget for the cooling rate profile both from prior knowledge and from knowledge gained by data from remote-sensing instruments. It is sensible to use a measure such as information content to compare these two states of knowledge.

[27] According to *Shannon* [1948], the information content can also be described by the entropy of the probability distribution functions associated with the a priori and aposteriori states. Given an assumption of Gaussian statistics for the quantity of interest, the entropy, and thus the information content can be directly related to the covariance matrix of the suite of physical variables estimated in the retrieval (e.g., T, $H_2O$, $O_3$ profiles):

$$S(P_a) = \frac{1}{2}\ln(|\mathbf{S}_a|) \tag{7}$$

where $P_a$ is the prior state and $\mathbf{S}_a$ is its associated covariance matrix. The information content $h$, in bits, is given by the difference in entropy from the prior to the posterior state:

$$h = -\frac{1}{2}\ln(|\hat{\mathbf{S}} * \mathbf{S}_a^{-1}|) \tag{8}$$

where $\hat{\mathbf{S}}$ is the posterior covariance matrix.

[28] We estimate the information content for the cooling rate profile derived from current thermal sounder measurements according to instrumental spectral coverage, noise, and resolution. The purpose of this analysis is to understand and compare how different instrument characteristics are able to impart knowledge toward the determination of the cooling rate profile. First, this analysis compares the cooling rate profile information, in bits, derived from standard optimal-estimation atmospheric state retrievals [*Rodgers*, 2000] for the temperature, $H_2O$, and $O_3$ profiles. While it is recognized that most operational retrieval techniques employ more advanced approaches to the inversion, a linear error analysis is chosen for simplicity and because the

**Table 1.** Comparison of Thermal Infrared Spectrometer Specifications and Cooling Rate Information Content for Different Model Atmosphere Conditions

| Instrument | Temporal Span | Spectral Coverage, $cm^{-1}$ | NeDT, K | Spectral Resolution, $cm^{-1}$ | $h_{TRP}$, bits | $h_{MLS}$, bits | $h_{SAW}$, bits |
|---|---|---|---|---|---|---|---|
| IRIS-D (Nimbus 4) | 1970–1971 | 400–1600 | 2–4 | 2.8 | 9.8 | 8.4 | 6.4 |
| AIRS (aqua) | 2002–Present | 650–1400, 1900–2700 | 0.1–0.6 | 1–2 | 17.1 | 11.5 | 12.6 |
| TES (aura) | 2004–Present | 650–1325, 1900–2250 | 1–4 | 0.12 | 13.2 | 10.5 | 8.0 |
| IASI | 2006–Present | 650–2700 | 0.3–0.5 | 0.5 | 21.8 | 19.9 | 18.3 |
| FIRST | Prototype | 50–2000 | 1.1 | 0.6 | 17.5 | 18.3 | 11.4 |

aposteriori covariance matrix estimation for nonlinear retrieval is similar to the linear case.

[29] For these cases, the suite of physical quantities retrieved consists of a vector of the concatenated profiles of the temperature and the logarithm of the $H_2O$, and $O_3$ profiles. We assume that the a priori covariance matrix for the gaseous profiles is given as a modification of equation (6), noting that a Taylor expansion approximation of the variance of a function is:

$$\mathrm{var}[f(x)] \approx (f'(x))^2 * \mathrm{var}(x) \tag{9}$$

which implies that for the transformation:

$$\begin{cases} y_i = \log(x_i) \\ y_j = \log(x_j) \end{cases} \tag{10a}$$

where $x_i$ and $x_j$ refer to gaseous profile concentration at different layers, that:

$$\begin{cases} \sigma(y_i) = \dfrac{\sigma(x_i)}{x_i} \\ \sigma(y_j) = \dfrac{\sigma(x_j)}{x_j} \end{cases} \tag{10b}$$

which leads to the following result for the $H_2O$ and $O_3$ elements of the a priori covariance matrix:

$$\mathrm{cov}(y_i, y_j) = \sigma(y_i)\sigma(y_j)\exp\left(-\frac{|z_i - z_j|}{H}\right) \tag{11}$$

The a priori covariance matrix is generally block-diagonal with respect to the different gaseous species in the absence of compelling a priori knowledge of the covariance between different profile quantities. That is, the retrieval of physical quantities can be implemented without constraining the covariance between different species though the covariance matrix of the suite of physical values retrieved from the measurement will not, in general, be block-diagonal. For information content analyses, the role of the a priori constraint is central toward determining how the measurement translates to total knowledge about the quantity of interest. Since the a priori was not specified rigorously here, it should be noted that for higher assumed values of prior uncertainty in T, $H_2O$, $O_3$ and correlations in those uncertainties, the information content associated with that measurement will also increase.

[30] The thermal infrared sounders herein compared include the IRIS-D instrument aboard the Nimbus 4 platform [*Hanel et al.*, 1971], the AIRS instrument aboard the Aqua platform [*Aumann et al.*, 2003], the TES instrument aboard the Aura platform [*Beer et al.*, 2001], the IASI instrument aboard the MetOp platform [*Chalon et al.*, 2001], and the FIRST instrument which is a newly-developed instrument that has been tested from a balloon platform [*Mlynczak et al.*, 2006]. All instruments are infrared spectrometers: AIRS, TES, and IASI measure most of the midinfrared out to approximately 650 $cm^{-1}$, while IRIS-D covers a portion of the far-infrared with measurements out to 400 $cm^{-1}$ and FIRST measures nearly the entire far-infrared out to 50 $cm^{-1}$. Each information content calculation requires the utilization of an instrument line shape (ILS). All but one of the instruments herein considered are Fourier Transform Spectrometers (FTS) and the ILS for the FTS instruments is specified as an upapodized sinc-function parameterized by the maximum optical path length of each scan and the integrated field of view. The specification of the ILS for the AIRS instrument, the only grating instrument included in the comparison, is defined by the postlaunch characterization of channel centroids and spectral response characteristics [*Gaiser et al.*, 2003]. The approximate noise characteristics of the instruments listed in Table 1 show the range of the Noise-Effective Delta Temperature (NeDT) for each instrument.

[31] A posteriori covariance of T, $H_2O$, and $O_3$ profiles is estimated according to a linear Bayesian atmospheric state retrieval approach detailed by *Rodgers* [2000] and is given by the following:

$$\hat{\mathbf{S}} = \left(\mathbf{K}^T\mathbf{S}_\varepsilon^{-1}\mathbf{K} + \mathbf{S}_a^{-1}\right)^{-1} \tag{12}$$

where $\mathbf{S}_\varepsilon$ is the measurement covariance matrix, *T* and *-1* denote the matrix transpose and inverse respectively, and $\mathbf{K}$ is the weighting function matrix with components given by:

$$K(i,j) = \frac{\partial R_i}{\partial x_j} \tag{13}$$

where $R_i$ refers to the radiance in the *i*th channel and $x_j$ is an input to the line-by-line radiative transfer model. The measurement covariance matrix is derived from an estimation of measurement error, which is generally acquired through a detailed calibration procedure. For this demonstration, static measurement error models were used which assume that the noise is limited to a non-spectrally correlated detector signal; that is, the off-diagonal elements

of the measurement covariance matrix are set to zero. While not all spectral errors are uncorrelated, it is reasonable to assume that in the course of the processing of raw detector data to geolocated, calibrated radiance data that a significant part of the calibration fluctuations and other spectrally-correlated errors can be corrected. The aposteriori covariance matrix from equation (11) is then re-entered into the cooling rate covariance matrix formulation calculated with equations (2) and (4) and from this, the cooling rate information content is calculated.

[32] Table 1 shows the information content of several clear-sky sounders for three model atmospheres [*Anderson et al.*, 1986] where $h_{TRP}$ denotes information content for the Tropical model atmosphere, $h_{MLS}$ denotes information content for the Mid-Latitude Summer model atmosphere, and $h_{SAW}$ denotes information content for the Sub-Arctic Winter model atmosphere. These results indicate some optimal qualities for remote sensing data for cooling rate profile determination. First, it is expected that older instruments such as IRIS-D with relatively low spectral resolution and high instrument noise will contain some information regarding the cooling rate profile, but that newer instruments will have improved performance. Second, the amount of information that a thermal sounder can derive about the cooling rate profile is also proportional to the thermal contrast between the surface and the atmosphere. Therefore, cooling rate profiles can be better determined when viewing tropical atmospheres as opposed to wintertime polar ones. Third, the balance between signal-to-noise ratio and spectral resolution tends to favor the AIRS instrument (which has a superior signal-to-noise ratio). Fourth, IASI, with comparable channel coverage and noise yet increased spectral resolution, should provide more information regarding the cooling rate profile as compared to AIRS. Finally, the descriptive ability of upper tropospheric water vapor bands that the FIRST instrument exhibits strongly suggests that far-infrared measurements do not represent a completely redundant description as compared to what is derived from the 6.3 $\mu$m $H_2O$ band. In fact, if only the midinfrared portion of the FIRST instrument is used for the analysis listed in Table 1, $h_{TRP}$ is 16.2 bits, $h_{MLS}$ is 16.9 bits, and $h_{SAW}$ is 10.3 bits. Moreover, it is expected that errors in the spectroscopic databases in the far-infrared will contribute to midtropospheric cooling rate profile biases and large-scale measurements in this spectral region should reveal discrepancies.

## 5. Concluding Remarks

[33] In this paper, we have addressed the formulation of a cooling rate profile error budget for clear-sky scenes. This is particularly important for cooling rate analysis from remote sensing data so that the errors associated with the retrieval of standard physical quantities are retained. We start with formal linear propagation of error analysis to derive an expression for the diagonal and off-diagonal components of the cooling rate profile covariance matrix. From this, we find that knowledge of the structure of error correlations in the T, $H_2O$, and $O_3$ profiles is important to the estimation of the cooling rate profile error budget in that higher error correlation tends to increase cooling rate uncertainty. While this knowledge may not always be available, it is necessary for the proper assessment of the cooling rate error budget.

[34] Next, we explore the assumptions made in the course of deriving an expression for the cooling rate covariance matrix are borne out by using a large set of T, $H_2O$, and $O_3$ profiles from the ERA-40 reanalysis data set. Namely, we test the extent to which linear error propagation can be assumed and Gaussian pdfs for radiative transfer model input variables can be utilized. There is qualitative agreement between the cooling rate profile covariance matrix derived from an ensemble of radiative transfer calculations and that derived from the covariance matrices of temperature, water vapor, and ozone profiles though some ad hoc second-order corrections may be required.

[35] Subsequently, we address how the formal retrieval of temperature, water vapor, and ozone profiles using thermal infrared spectra impart information toward understanding the clear-sky cooling rate profiles. Several spectrometers were compared with different spectral coverage, resolution, signal-to-noise ratio. Among operational spectrometers, IASI was found to have the ability to provide the greatest amount of information to the cooling rate profile; also, it was found that it may be scientifically useful to develop far-infrared missions in terms of cooling rate profile analysis. In the absence of operational far-infrared satellite-borne spectrometer, the implicit information contained in midinfrared spectra about long-wavelength processes will have to suffice.

[36] This paper has not directly discussed the characterization of cooling rate errors and their correlations in GCMs and reanalysis data. However, with the uncertainties in T, $H_2O$, and $O_3$ profiles, the cooling rate error propagation described herein can be applied. Straightforward statistical tests can be employed to test the significance of discrepancies between cooling rates derived from satellite-based products and those calculated in circulation models.

[37] One major frontier in the characterization of the cooling rate profile error budget is how uncertainties in cloud cover and overlap impact the error budget formulation in this paper. Thermal IR spectra may be able to provide partial information regarding cloud-covered scenes, but most of that information will be imparted toward cooling rate profiles above the cloud decks. The cooling rate profiles arising from the new generation of active remote sensing instruments in the A-Train including CloudSat [*Stephens et al.*, 2002] and Calipso [*Winker et al.*, 2003] should be able to provide large amounts of information on the cooling rate profile. Since different cloud vertical distributions produce differential changes in $H_2O$ rotational band cooling and $O_3$ $\nu_3$ and $\nu_1$ IR heating [e.g., *Hartmann et al.*, 2001] which may affect such processes as stratosphere-troposphere exchange [*Gettelman et al.*, 2004; *Fueglistaler and Fu*, 2006], cloud water content and optical depth profiles will impart unprecedented information on heating/cooling rate profiles at high vertical resolution. The work of *L'Ecuyer* [2001] may prove to be very useful for addressing the cooling rate error budget in the presence of clouds, and the advent of the 2B-FLXHR product associated with CloudSat [*L'Ecuyer*, 2007] presents a comprehensive assessment of cloud radiative impacts throughout the atmospheric column. Significant IR radiative heating generally occurs at cloud bases and cooling occurs at cloud tops with rates as high as 100 K/d

for sharp cloud boundaries; therefore, it is expected that error budget determination for cooling rates in all-sky scenes will require that more attention be focused on the linearity and Gaussian pdf assumptions utilized here.

[38] Finally, methods for determining shortwave heating rate profiles have not been discussed though they are of course necessary to the determination of the layer-by-layer radiative energetic budget. The formal error propagation discussion herein is directly relevant to clear-sky heating rate error budget analyses.

[39] **Acknowledgments.** This research was supported by the NASA Earth Systems Science Fellowship, grant NNG05GP90H. Yung was supported by NASA grant to JPL under the MAP program. Invaluable technical support was provided by Tony Clough, Mark Iacono, and Mark Shepard at AER, Inc. Other support was provided by Marty Mlynczak and David Johnson of the NASA Langley Research Center. The author would also like to acknowledge the help provided by the Yuk Yung Radiation Group including Jack Margolis, Vijay Natraj, Xin Guo, Kuai Le, King-Fai Li, Mao-Chang Liang, and Ross Cheung. Finally, this work benefited immensely from the comments of the three anonymous reviewers.

## References

Anderson, G. P., S. A. Clough, F. X. Kneizys, J. H. Chetwynd, and E. P. Shettle (1986), AFGL atmospheric constituent profiles (0–120 km), *AFGL-TR_86-0110*, Hanscom AFB, Mass.

Aumann, H. H., et al. (2003), AIRS/AMSU/HSB on the aqua mission: Design, science objectives, data products, and processing systems, *IEEE Trans. Geosci. Remote Sens.*, *41*, 253–264.

Baer, F., N. Arsky, J. J. Charney, and R. G. Ellingson (1996), Intercomparison of heating rates generated by global climate model longwave radiation codes, *J. Geophys. Res.*, *101*(D21), 26,589–26,603.

Barnet, C. D., S. Datta, and L. Strow (2003), Trace Gas measurements from the Atmospheric Infrared Sounder (AIRS), *Optical Remote Sensing*, Optical Society of America (OSA) Technical Digest, paper OWB2.

Beer, R., T. A. Glavich, and D. M. Rider (2001), Tropospheric emission spectrometer for the Earth Observing System's Aura satellite, *Appl. Opt.*, *40*, 2356–2367.

Bergman, J. W., and H. H. Hendon (1998), Calculating monthly radiative fluxes and heating rates from monthly cloud observations, *J. Atmos. Sci.*, *55*, 3471–3491.

Chalon, G., et al. (2001), IASI: An advanced sounder for operational meteorology, paper presented at 52nd Congress of the IAF, Toulouse, France, 1–5 Oct. 2001.

Clough, S. A., and M. J. Iacono (1995), Line-by-line calculations of atmospheric fluxes and cooling rates: 2. Application to carbon dioxide, ozone, methane, nitrous oxide, and the halocarbons, *J. Geophys. Res.*, *100*, 16,519–16,535.

Clough, S. A., and F. X. Kneizys (1966), Coriolis interaction in V1 and V3 fundamentals of ozone, *J. Chem. Phys.*, *44*, 1855.

Clough, S. A., M. J. Iacono, and J. L. Moncet (1992), Line-by-line calculation of atmospheric fluxes and cooling rates: Application to water vapor, *J. Geophys. Res.*, *97*(D14), 15,761–15,785.

Clough, S. A., M. W. Shephard, E. Mlawer, J. S. Delamere, M. Iacono, K. Cady-Pereira, S. Boukabara, and P. D. Brown (2005), Atmospheric radiative transfer modeling: A summary of the AER codes, *J. Quant. Spectrosc. Radiat. Transfer*, *91*(2), 233–244.

Collins, W. D., et al. (2006), Radiative forcing by well-mixed greenhouse gases: Estimates from climate models in the Intergovernmental Panel on Climate Change (IPCC) Fourth Assessment Report (AR4), *J. Geophys. Res.*, 111, D14317, doi:10.1029/2005JD006713.

Ellingson, R. G., and Y. Fouquart (1991), The intercomparison of radiation codes in climate models - An overview, *J. Geophys. Res.*, *96*, 8925–8927.

Feldman, D. R., K. N. Liou, Y. L. Yung, D. C. Tobin, and A. Berk (2006), Direct retrieval of stratospheric CO2 infrared cooling rate profiles from AIRS data, *Geophys. Res. Lett.*, *33*, L11803, doi:10.1029/2005GL024680.

Fisher, R. A. (1925), Theory of statistical estimation, *Proc. Cambridge Philos. Soc.*, *22*, 700–725.

Fueglistaler, S., and Q. Fu (2006), Impact of clouds on radiative heating rates in the tropical lower stratosphere, *J. Geophys. Res.*, 111, D23202, doi:10.1029/2006JD007273.

Gaiser, S. L., H. H. Aumann, L. L. Strow, S. Hannon, and M. Weiler (2003), In-flight spectral calibration of the atmospheric infrared sounder, *IEEE Trans. Geosci. Remote Sens.*, *41*, 287–297.

Gettelman, A., P. M. de Forster, F. Fujiwara, M. Fu, Q. Vömel, H. Gohar, L. K. Johanson, and C. Ammerman (2004), Radiation balance of the tropical tropopause layer, *J. Geophys. Res.*, *109*, D07103, doi:10.1029/2003JD004190.

Goody, R. M., and Y. L. Yung (1989), *Atmospheric Radiation Theoretical Basis*, 519 pp., Oxford Univ. Press, New York.

Hanel, R. A., B. Schlachman, D. Rogers, and D. Vanous (1971), Nimbus 4 Michelson interferometer, *Appl. Opt.*, *10*, 1376–1382.

Hartmann, D. L., J. R. Holton, and Q. Fu (2001), The heat balance of the tropical tropopause, cirrus, and stratospheric dehydration, *Geophys. Res. Lett.*, *28*(10), 1969–1972, doi:10.1029/2000GL012833.

Iacono, M. J., E. J. Mlawer, S. A. Clough, and J.-J. Morcrette (2000), Impact of an improved longwave radiation model, RRTM, on the energy budget and thermodynamic properties of the NCAR community climate model, CCM3, *J. Geophys. Res.*, *105*(D11), 14,873–14,890, doi:10.1029/2000JD900091.

Kratz, D. P., et al. (2005), An inter-comparison of far-infrared line-by-line radiative transfer models, *J. Quant. Spectrosc. Radiat. Transfer*, *90*, 323–341.

L'Ecuyer, T. S. (2001), Uncertainties in Space-Based Estimates of Clouds and Precipitation: Implications for Deriving Global Diabatic Heating, Ph.D. thesis in Atmospheric Science, Colorado State University.

L'Ecuyer, T. S. (2007), Level 2 fluxes and heating rates product process description and interface control document, v. 5, http://www.cloudsat.cira.colostate.edu/ICD/2B-FLXHR/flxhr2b_icd_v5.pdf, CloudSat Data Processing Center, Fort Collins, Colorado.

Li, J., et al. (2005), Retrieval of cloud microphysical properties from MODIS and AIRS, *J. Appl. Meteorol.*, *44*, 1526–1543.

Liou, K. N. (2002), *An Introduction to Atmospheric Radiation*, 2nd ed., 583 pp., Elsevier, New York.

Liou, K. N., and Y. K. Xue (1988), Exploration of the remote sounding of infrared cooling rates due to water-vapor, *Meteorol. Atmos. Phys.*, *38*(3), 131–139.

McFarlane, S. A., J. H. Mather, and T. P. Ackerman (2007), Analysis of tropical radiative heating profiles: A comparison of models and observations, *J. Geophys. Res.*, *112*, D14128, doi:10.1029/2006JD008290.

Mlawer, E. J., S. J. Taubman, P. D. Brown, M. J. Iacono, and S. A. Clough (1997), Radiative transfer for inhomogeneous atmospheres: RRTM, a validated correlated- k model for the longwave, *J. Geophys. Res.*, *102*(D14), 16,663–16,682.

Mlynczak, M. G., C. J. Mertens, R. R. Garcia, and R. W. Portmann (1999), A detailed evaluation of the stratospheric heat budget: 2. Global radiation balance and diabatic circulations, *J. Geophys. Res.*, *104*(D6), 6039–6066.

Mlynczak, M. G., et al. (2006), First light from the Far-Infrared Spectroscopy of the Troposphere (FIRST) instrument, *Geophys. Res. Lett.*, *33*, L07704, doi:10.1029/2005GL025114.

Morcrette, J. J. (1990), Impact of changes to the radiation transfer parameterizations plus cloud optical properties in the ECMWF model, *Mon. Weather Rev.*, *118*, 847–873.

Palacios, M. B., and M. F. J. Steel (2006), Non-Gaussian Bayesian geostatistical modeling, *J. Am. Stat. Assoc.*, *101*, 604–618.

Posselt, D. J., T. S. L'Ecuyer, and G. L. Stephens (2006), Nonlinear non-Gaussian parameter estimation using Markov chain Monte Carlo methods, *Eos Trans. AGU*, *87*(52), Fall Meet. Suppl., Abstract A31A-0867.

Qu, Y. N., et al. (2001), Ozone profile retrieval from satellite observation using high spectral resolution infrared sounding instrument, *Adv. Atmos. Sci.*, *18*, 959–971.

Rodgers, C. D. (2000), *Inverse Methods for Atmospheric Sounding: Theory and Practice*, 238 pp., World Sci., Hackensack, N. J.

Shannon, C. E. (1948), A mathematical theory of communication, *Bell Syst. Tech. J.*, *27*, 379–423, 623–656.

Sherwood, S. C., and A. E. Dessler (2001), A model for transport across the tropical tropopause, *J. Atmos. Sci.*, *58*, 765–779.

Stephens, G. L., et al. (2002), The Cloudsat mission and the A-train - A new dimension of space-based observations of clouds and precipitation, *Bull. Am. Meteorol. Soc.*, *83*, 1771–1790.

Susskind, J., et al. (2006), Accuracy of geophysical parameters derived from Atmospheric Infrared Sounder/Advanced Microwave Sounding Unit as a function of fractional cloud cover, *J. Geophys. Res.*, 111, D09517, doi:10.1029/2005JD006272.

Taylor, B. N., and C. E. Kuyatt (1994), *Guidelines for Evaluating and Expressing the Uncertainty of NIST Measurement Results*, NIST Technical Note 1297, http://www.physics.nist.gov/Pubs/guidelines/contents.html, National Institute of Standards and Technology, Gaithersburg, Maryland.

Uppala, S. M., et al. (2005), The ERA-40 re-analysis, *Q. J. R. Meteorol. Soc.*, *131*, 2961–3012.

Winker, D. M., J. Pelon, and M. P. McCormick (2003), The CALIPSO mission: Spaceborne lidar for observation of aerosols and clouds, *Proc. SPIE*, *4893*, 1–11.

Zhang, Y. C., W. B. Rossow, and A. A. Lacis (1995), Calculation of surface and top of atmosphere radiative fluxes from physical quantities based on ISCCP data sets: 1. Method and sensitivity to input data uncertainties, *J. Geophys. Res.*, *100*, 1149–1165.

Zhang, Y. C, W. B. Rossow, A. A. Lacis, V. Oinas, and M. I. Mishchenko (2004), Calculation of radiative fluxes from the surface to top of atmosphere based on ISCCP and other global data sets: Refinements of the radiative transfer model and the input data, *J. Geophys. Res.*, *109*, D19105, doi:10.1029/2003JD004457.

D. R. Feldman, Department of Environmental Science and Engineering, California Institute of Technology, 1200 East California Boulevard, MC 150-21, Pasadena, CA 91125, USA. (feldman@caltech.edu)

K. N. Liou, Department of Atmospheric and Oceanic Sciences, University of California-Los Angeles, 405 Hilgard Ave., Los Angeles, CA 90095-1565, USA.

R. L. Shia and Y. L. Yung, Division of Geological and Planetary Sciences, California Institute of Technology, 1200 E California Blvd., MC 150-21 Pasadena, CA 91125, USA.